Research Article

Preparation of Anodic Aluminum Oxide Masks with Size-Controlled Pores for 2D Plasmonic Nanodot Arrays

Mi Jung [iD],[1] **Ji-Hoon Kim**,[2] **and Young-Wan Choi** [iD][2]

[1]*Institute of Innovative Functional Imaging, Chung-Ang University, Seoul 06974, Republic of Korea*
[2]*School of Electrical and Electronics Engineering, Chung-Ang University, Seoul 06974, Republic of Korea*

Correspondence should be addressed to Young-Wan Choi; ychoi@cau.ac.kr

Anodic aluminum oxide (AAO) layers with nano-sized pores have been used as shadow masks for the fabrication of two-dimensional (2D) metal nanodot arrays (NDAs). However, the localized surface plasmon resonance (LSPR) of size-controlled NDAs fabricated using AAO masks has not been much studied. In this study, we report on the improved preparation method and utilization of an ultrathin AAO mask for the fabrication of 2D plasmonic metal NDAs. The greatest challenge in preparing an AAO mask is to control the pore diameter and to make it reproducible. AAO masks with size-controlled pores were reproducibly prepared using a two-step chemical wet etching method. Ag NDAs with different dot diameters (42, 60, and 80 nm) and Ag, Cu, and Au NDAs with dot a diameter of 80 ± 5 nm were fabricated on indium tin oxide glass substrates using AAO masks. The wavelengths corresponding to LSPR of 2D metal NDAs were investigated using ultraviolet–visible spectroscopy. Our results show that AAO masks with tunable pores can be used as shadow masks for the fabrication of 2D plasmonic NDAs.

1. Introduction

Fabrication techniques for two-dimensional (2D) plasmonic nanodot arrays (NDAs) have attracted significant attention in versatile plasmonic applications for the enhancement of the performance of optoelectronic devices and for the highly sensitive detection of biological and chemical sensors [1–3]. The localized surface plasmon resonance (LSPR) of metal nanoparticles is sensitive to parameters such as shape, size, composition, and the surrounding environment [4–6]. Along with the development of nanostructure manufacturing technology, research on various plasmonic applications based on the LSPR of metal nanostructures has been proceeding rapidly [7–12]. Plasmonic nanosensors have been utilized to detect chemical and biomolecular binding on metal surfaces by measuring extremely small wavelength shifts in LSPR owing to a change in the refractive index [7–9]. Plasmonic properties of metal nanoparticles have been investigated to improve the performance of optoelectronic devices such as organic light-emitting diodes (OLEDs), solar cells, and light-emitting diodes [10–12].

In addition, the LSPR features depending on the shape and size of metal nanostructures have a significant influence on the characterizations of optoelectronic devices such as the change of emission color in OLEDs, the conversion efficiency of solar energy, and the activity of catalyst [13–15]. Specifically, metal nanoparticle arrays exhibit much higher electromagnetic field enhancements than those of single-insulated nanoparticles and are easy to reproducibly produce in the desired region [16, 17]. Thus, manufacturing techniques that can reproduce a metal nanoparticle array on a substrate are important for optimizing the performance in plasmonic applications.

2D nanoparticle arrays such as Au disk, Ag disk, and ellipsoidal Au nanoparticles with different lattice constants have been achieved using electron beam lithography [17, 18]. This technique facilitates the control of the geometric pattern of nanoparticles, but it has some drawbacks such as high cost and large-area patterning. Owing to these limitations, 2D metal nanoparticle arrays have been fabricated by nonlithographic techniques using self-organized nanostructured materials as a template [4, 8–11, 19–27]. Among the
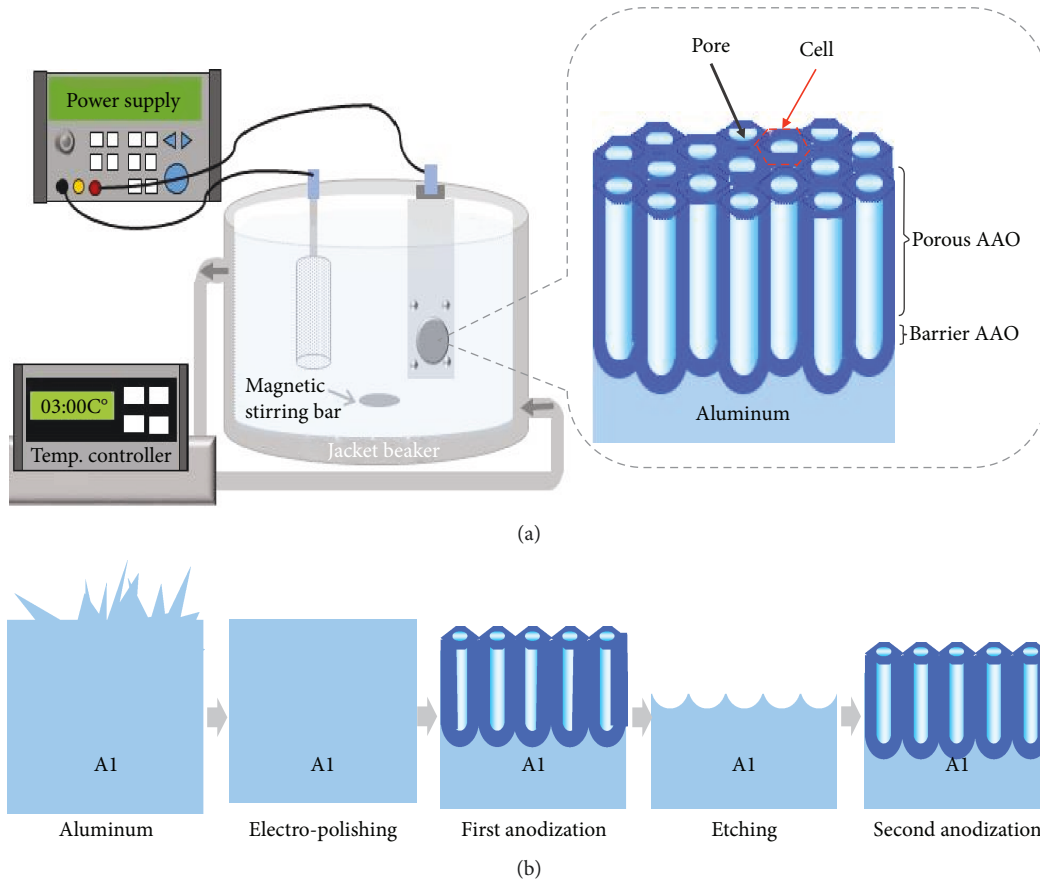
(a)

(b)

FIGURE 1: Schematic illustrations depicting the structure and the fabrication process for a well-ordered AAO layer: (a) the equipment configuration for the anodization method used in this work and (b) each experimental stage of the two-step anodization process.

materials, a self-organized anodic aluminum oxide (AAO) layer with uniform through holes of nanometer dimensions has been widely used as a shadow mask to fabricate 2D NDAs of various materials [20–27]. However, the plasmonic properties of metal NDAs produced using AAO masks have not been reported widely. Several studies have reported the LSPR of Ag or Au NDAs with height variations by varying the amount of metal deposited using AAO masks with similar pore diameters [24–26]. However, the LSPR of metal NDAs with different diameters of similar height has not yet reported due to the difficulty of controlling the pore diameter of the AAO mask. The most challenges in preparing the AAO mask are to completely remove the barrier layer at the bottom and control the pore diameter. In order to obtain an ultrathin AAO mask, the removal of the barrier layer and pore widening were performed by chemical etching in 5% H_3PO_4 or by Ar^+ milling [24–30]. The Ar^+ ion milling method for the barrier layer removal is expensive and time-intensive [28]. Removing the barrier layer through long-term chemical etching is difficult to control the size of the pores because the AAO mask tends to break or crack [29]. In this study, we demonstrate an improved preparation method of AAO masks with adjustable pore diameters for the fabrication of size-controlled 2D NDAs. AAO masks were prepared by a two-step chemical wet

etching method as reported previously [24]. The pore diameters of AAO masks were adjusted by controlling the dipping time in the second chemical wet etching process. Ag NDAs with different dot diameters and Ag, Cu, and Au NDAs with similar dot diameters were fabricated on indium tin oxide (ITO) substrates using AAO masks with size-controlled pores. The chemical structures of metal NDAs were examined by X-ray photoelectron spectroscopy (XPS). The plasmonic properties of metal NDAs were investigated using ultraviolet–visible spectroscopy.

2. Experiments

2.1. Preparation of AAO Mask. The surface of the aluminum foil was pretreated using electrolytic polishing at 20 V for 60 s in a solution of perchloric acid and ethanol ($HClO_4 : C_2H_6O = 1 : 5$ (in volume ratio)). The aluminum foil inserted in a sample holder made of Teflon was connected to the anode, and the platinum electrode was connected to the cathode. Figure 1(a) shows the schematic diagrams of the equipment configuration for the anodization method and the structure of the AAO layer formed on the aluminum foil by the anodization method. Figure 1(b) shows the schematic diagrams of the two-step anodization process. The first anodization was performed in a 0.3 M oxalic acid

($H_2C_2O_4$) solution for 6 h by applying a constant dc voltage of 40 V. A magnetic stir bar was rotated at a constant speed at the bottom of the jacket beaker containing the solution to remove the heat generated during the anodization process. For low growth rates of the AAO layer, the temperature of the solution was maintained at 3°C using a refrigerated water circulator. The AAO layer formed during the first anodization process was dissolved in a mixed solution of 0.4 M phosphoric acid (H_3PO_4) and 0.2 M chromic acid (H_2CrO_4) at 65°C for approximately 6 h. The second anodization was performed for 240 s under the same conditions as those of the first anodization. The AAO layer was etched slightly via immersion for 600 s in 5 wt% phosphoric acid at 30°C following the second anodization. The surface of the AAO layer was subsequently coated with a solution containing a mixture of nitrocellulose and polyester resin in butyl acetate, ethyl acetate, and isopropyl alcohol. The remaining aluminum substrate was removed using a saturated mercuric chloride ($HgCl_2$) solution for approximately 4 h. The pore diameters of AAO masks were adjusted by controlling the dipping time in the second chemical wet etching process. Finally, the coating layer on the AAO surface was dissolved in acetone. Subsequently, the AAO mask was filtered using a filter paper.

2.2. Fabrication of Plasmonic NDAs. The AAO mask was placed on an ITO substrate, which was subsequently placed on a sample holder in the evaporator chamber. Metal was deposited on the surface of the ITO substrate covered with the AAO mask by using an electron beam evaporator (ULVAC EBX-1000). Under a vacuum of $\sim 10^{-4}$ Torr, metals such as Ag, Cu, and Au were deposited at a deposition rate of ~0.1 nm/s for 500 s. Under these deposition conditions, the thickness of the metal film deposited on the ITO substrate without an AAO mask was approximately 50 nm. After the deposition of each metal, the mask on the ITO substrate was selectively dissolved in 1 M sodium hydroxide (NaOH) for several minutes and rinsed several times with distilled water. Thus, Ag, Cu, and Au NDAs were formed on the ITO substrate.

2.3. Characterizations. The morphologies of the AAO mask and metal NDAs were observed using a field-emission scanning electron microscope (FE-SEM; Hitachi S-4700) and atomic force microscope (AFM; Park Systems XE-100). The chemical compositions and electronic structures of the metal NDAs were confirmed using XPS (PHI 5000 Versa Probe, ULVAC-PHI Inc.). The XPS measurements were performed using microfocused ($100\,\mu m \times 100\,\mu m$, 25 W, 15 kV) monochromatic Al Kα radiation with an energy of 1486.6 eV. The instrument was calibrated to provide a C1s binding energy of 284.6 eV. The pressure inside the analyzer was maintained at 5×10^{-10} Torr. The plasmonic properties of the metal NDAs were measured using a UV–Vis spectrometer (Perkin Elmer Lambda 18) in a wavelength range of 270–900 nm. The sample was placed behind a collimator lens and on a position-controlled stage, and the extinction measurement was recorded using unpolarized light with a probe beam size of approximately 4 mm^2.

3. Results and Discussion

3.1. Preparation of AAO Mask. The AAO layer was prepared from an aluminum foil by the two-step anodization process reported by Masuda and Satoh [22]. After the second anodization, the AAO layer was immersed once in the phosphoric acid solution, and then the pore diameter of the AAO mask was controlled by varying the immersion time in the second etching process. The AAO mask with size-controlled pores was prepared by a two-step wet etching process, which was designed with the hint in the two-step anodization method. Figure 2 shows schematic illustrations and FE-SEM images of the pore opening process of the AAO layer using the two-step wet etching method. Figure 2(a) shows the FE-SEM image of the cross-sectional view of the AAO layer formed via the second anodization for 4 min. The structure of the AAO layer was composed of a porous layer and barrier layer on the aluminum substrate. The porous layer consisted of densely packed cylindrical pores perpendicular to the barrier layer. The thickness of the AAO layer was approximately 250 nm. The barrier layer at the bottom of the AAO layer had a uniform thickness of 46 ± 3 nm for each cell. The close-packed hexagonal cell size of the AAO layer is approximately 105 ± 5 nm. After the first wet etching conducted in 5 wt% H_3PO_4 solution for 600 s, the barrier layer thickness at the bottom of the AAO layer is approximately 26 nm as shown in Figure 2(b). In a comparison of Figures 2(a) and 2(b), Figure 2(b) clearly shows a thinner barrier thickness. Figure 2(c) shows the FE-SEM image of the bottom of the alumina barrier layer after the remaining aluminum substrate was dissolved in a saturated $HgCl_2$ solution after the first wet etching for 600 s. The most important step in preparing an AAO mask is to completely remove the barrier AAO layer and to open the pores. After the first wet etching, the surface of the AAO layer was coated with the coating layer, and the remaining aluminum substrate was removed using a saturated $HgCl_2$ solution. In the second wet etching process, the AAO layer was immersed again in 5 wt% H_3PO_4 solution for 690 s. Figure 2(d) shows the FE-SEM image of the AAO mask after the removal of the protecting layer in acetone. As shown in Figure 2(d), it was confirmed that the barrier AAO layer was completely dissolved. The pores were widened uniformly, and the average diameter of the pores was approximately 60 nm (± 5 nm).

3.2. Metal NDAs Using AAO Masks. Ultrathin, large-area AAO masks could be prepared using a two-step wet etching process. Au was deposited on an ITO substrate covered with an AAO mask for 500 s at a deposition rate of 0.1 nm/s. Figure 3(a) shows the FE-SEM image of Au-deposited AAO mask and Au NDA revealed from which the AAO mask was partially stripped with a carbon tape. Figure 3(b) shows the FE-SEM image of Au NDA after removing the AAO mask with a carbon tape. Figure 3(c) shows the interface between the Au-deposited mask surface and the Au NDA after the AAO mask is partially removed. Figure 3(d) shows that Au clusters were deposited on the top surface of the AAO mask as a replica of the pore pattern of the mask. Under
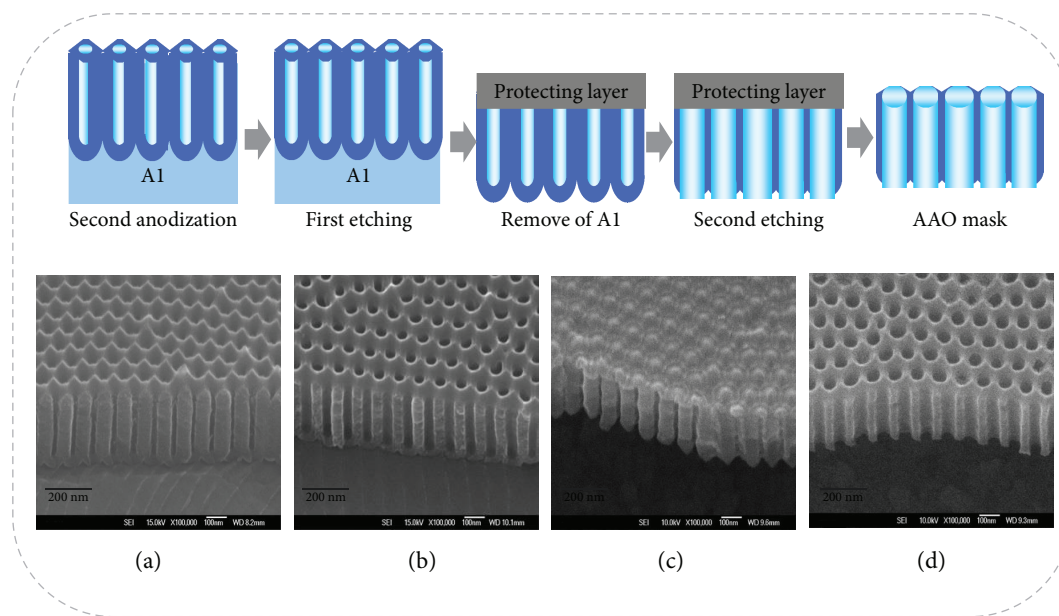
FIGURE 2: Schematic illustrations depicting the two-step wet etching process. FE-SEM images show the AAO layer prepared in the pore opening process using the method: (a) the second anodization for 4 min, (b) the first chemical wet etching for 10 min, (c) the bottom part of the AAO layer after dissolving the remaining aluminum substrate in a saturated HgCl$_2$ solution, and (d) the AAO layer with through pores after the second wet etching for 11 min.

the deposition rate of 0.1 nm/s, it can be observed that Au was uniformly deposited without blocking the nanopores of the AAO mask.

Figure 4(a) shows that the pore diameter of the AAO mask etched by the second dipping for 600 s was 43 nm (±5 nm) after the first wet etching for 600 s. Figures 4(b) and 4(c) show the FE-SEM images of the AAO mask with different pore diameters depending on the second wet etching time, that is, 60 nm (±5 nm) for the dipping time of 690 s and 80 nm (±5 nm) for the dipping time of 780 s. After the deposition of Ag, the AAO masks were dissolved in 1 M NaOH solution. The Ag NDAs with size-controlled diameters of 45 ± 5 nm (Figure 4(d)), 60 ± 5 nm (Figure 4(e)), and 80 ± 5 nm (Figure 4(f)) were fabricated using the AAO masks with different pore diameters. After the first wet etching for 600 s, the pore diameters of the AAO masks could be controlled by varying the dipping time.

Figures 5(a)–5(c) show the topology of Ag NDAs with different dot sizes investigated using AFM. The cross-sectional line profile along the red line in the AFM topographic image of Ag NDA is shown in Figure 5(a), with an average height of 20 ± 5 nm corresponding to the dots on the line. The mean diameter of Ag NDA formed on the ITO substrate was 45 ± 5 nm. Figure 6(b) shows the cross-sectional line profile along the red line in the AFM topology image of the curve, with an average height of 22 ± 5 nm corresponding to the vertices of two points on this line. The mean diameter of Ag NDA was 60 ± 5 nm. In the curved AFM topology image, the cross-sectional line profile along the red line is shown in Figure 5(c), with an average height of 18 ± 4 nm corresponding to the two vertices of the point. The average diameter of Ag NDA was 80 ± 5 nm. Considering the variation in height at the nanolevel of the surface of

the coated ITO substrate, it can be observed that the results were produced at approximately the same height. The dot heights of Ag NDA depend on the aspect ratio of the AAO mask and the amount of the deposited metal [20, 26]. Thus, it can be observed that AAO masks were manufactured under similar conditions.

Figures 6(a)–6(c) show the FE-SEM images of Ag, Cu, and Au NDAs with similar diameters that were fabricated on ITO substrates using AAO masks with a pore diameter of 80 ± 5 nm. The average diameter of the metal NDAs was 80 ± 5 nm as a replica of the AAO mask. The chemical composition and bonding states of Ag, Cu, and Au NDAs were studied using XPS. The binding energies were referenced to the C1s line, which was at 284.6 eV from carbon. As shown in Figure 6(d), the XPS spectra obtained from Ag NDA were centered at 368.2 and 374.2 eV. These values are consistent with the Ag $3d_{5/2}$ and Ag $3d_{3/2}$ core-level binding energies for the Ag nanoparticles appearing at 368.1 and 374.1 eV [31]. The separation value between the Ag $3d_{5/2}$ and Ag $3d_{3/2}$ transitions exhibits a spin orbital splitting of 6.0 eV, which is a characteristic of metallic silver [32]. Figure 6(e) shows the XPS spectra obtained from Cu NDA. The XPS spectra of Cu $2p_{3/2}$ at 932.4 eV and $2p_{1/2}$ at 952.4 eV confirm the presence of metallic copper [33, 34]. Otherwise, the two dominant peaks were Cu $2p_{1/2}$ at 953.9 eV with an intense satellite at 962.5 eV and $2p_{3/2}$ at 934.4 eV with an intense satellite at 941.2 eV, which are the peaks corresponding to CuO and copper hydroxide (Cu(OH)$_2$). Copper hydroxide usually displays the Cu $2p_{3/2}$ spectrum in the range of 934 to 936 eV [34, 35]. The values of the Cu $2p_{3/2}$ binding energies for Cu metals, CuO, Cu(OH)$_2$, and Cu$_2$O obtained from previous literature are 932.67, 932.6, 933.7, and 934.9 eV, respectively [36].
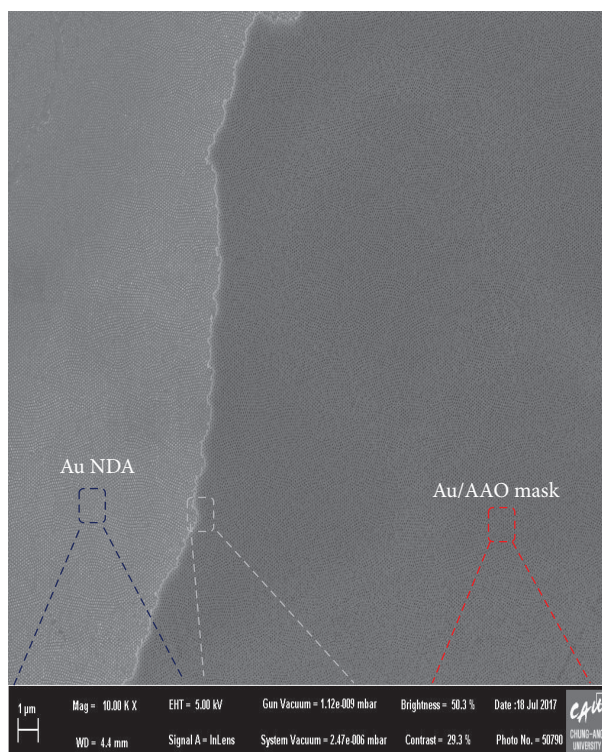
(a)
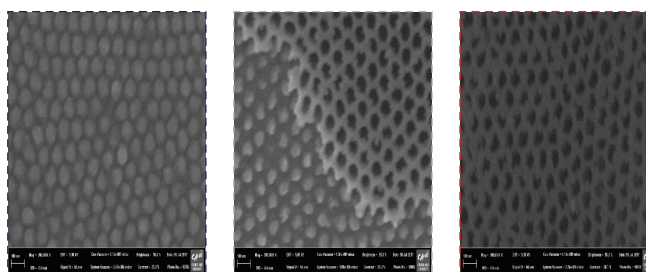
(b)

(c)

(d)

FIGURE 3: FE-SEM images of (a) Au-deposited AAO mask and Au NDA after a portion of the AAO mask was removed with a carbon tape, (b) Au NDA, (c) the boundary between the Au-deposited AAO mask and Au NDA, and (d) Au clusters deposited on top of the AAO mask.

These results indicate that copper hydroxide was formed on the surfaces of the Cu NDA during the process of dissolution of the AAO mask in aqua solution. As shown in Figure 6(f), the Au $4f_{7/2}$ and Au $4f_{5/2}$ core-level binding energies for Au NDA were observed at 84.1 and 87.9 eV. The binding energy of Au $4f_{7/2}$ for metallic gold was observed at 84.0 eV [37]. The binding energies of Au $4f_{7/2}$ and Au $4f_{5/2}$ for the Au NDA were observed at 84.7 and 88.3 eV, respectively [16]. The slight difference in the XPS peak position may be due to the changes in binding energy because of the particle shape or local chemical composition on the sample surface [37]. Thus, the material components of plasmonic NDAs were confirmed using XPS measurement.

3.3. Plasmonic Properties of Metal NDAs. The extinction spectrum, which is the sum of the absorption and scattering spectra, of metal NDA was measured in transmission mode using UV–Vis spectroscopy. The optical extinction has a

maximum at the plasmon resonant frequency, which corresponds to the LSPR peak of noble metal nanoparticles appearing in the visible wavelength range [6]. Figure 7(a) shows the LSPR spectra of Ag NDAs with different dot diameters in the period of 105 nm. The LSPR spectrum of the Ag NDA with a diameter of 45 ± 5 nm indicates the maximum peak at 498 nm. The spectra of the Ag NDAs with diameters 60 ± 5 nm and 80 ± 5 nm indicate the maximum peaks at 516 nm and 533 nm. As shown in Figure 7(a), the LSPR peak position is observed at different positions depending on the Ag dot size, shifting to the red region as the Ag nanodot diameter increases. The LSPR intensity of an Ag NDA with larger dots is higher than that with smaller dots. The LSPR peak broadening for Ag NDA on the substrate becomes larger as the diameter of the nanodots increased. The linewidth and the amplitude of the LSPR peaks depend on the size distribution and the distances between the particles [38, 39]. Our results are similar to those of the previous
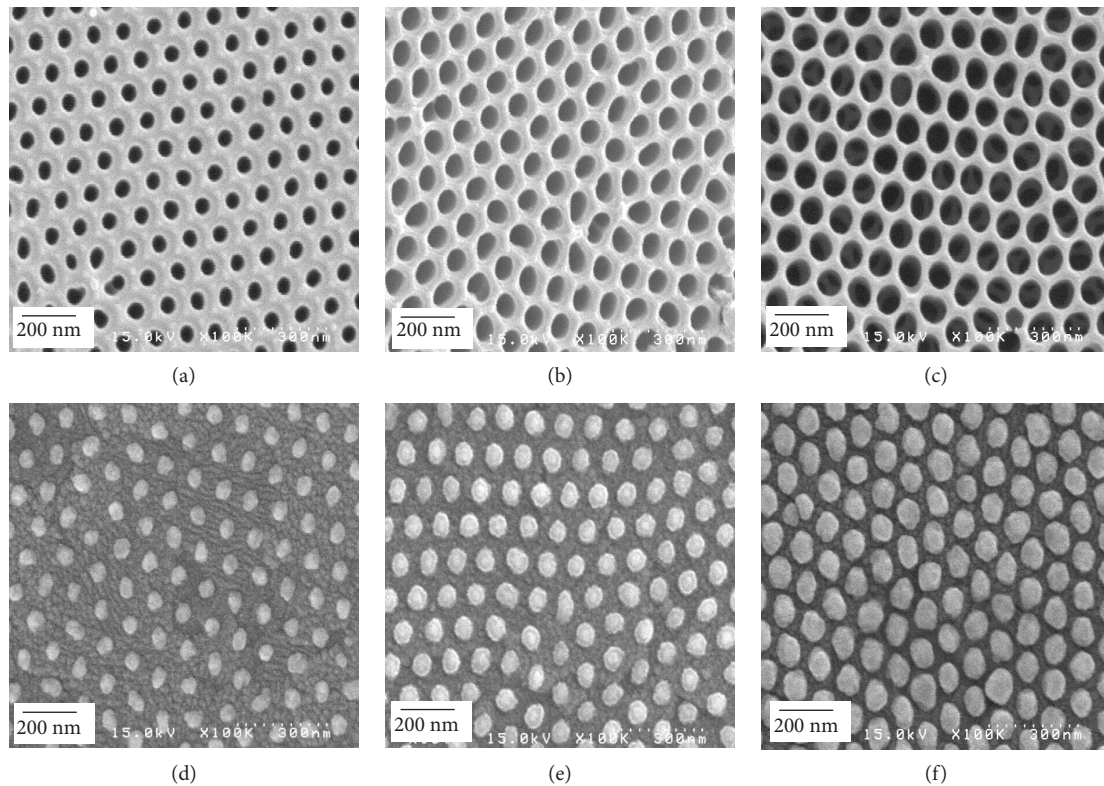
FIGURE 4: FE-SEM images of the AAO mask with different diameters: (a) 45 nm, (b) 60 nm, and (c) 80 nm. FE-SEM images of Ag NDAs with different diameters—(d) 42 nm, (e) 60 nm, and (f) 80 nm—formed on ITO substrates.
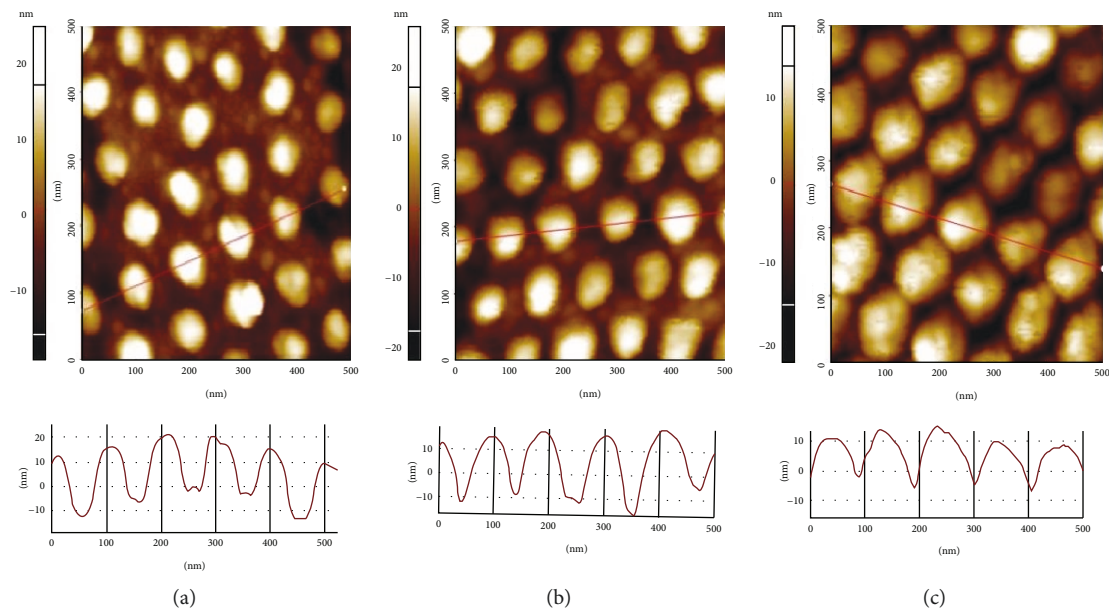

FIGURE 5: 2D AFM images of top views and cross-sectional line profiles in red lines of Ag NDAs with different diameters: (a) 45 nm, (b) 60 nm, and (c) 80 nm.

studies in which the LSPR wavelength shifts to red and the peak broadens as the particle size increases [4, 18]. Figure 7(b) shows the LSPR spectra of Ag, Cu, and Au NDAs with similar dot diameters of 80 ± 5 nm. Although

the sizes of metal NDAs were similar, the maximum peaks of LSPR were observed at different positions depending on the native element of the metal. The spectrum for the Ag NDA shows the maximum peak at 533 nm. For the spectra
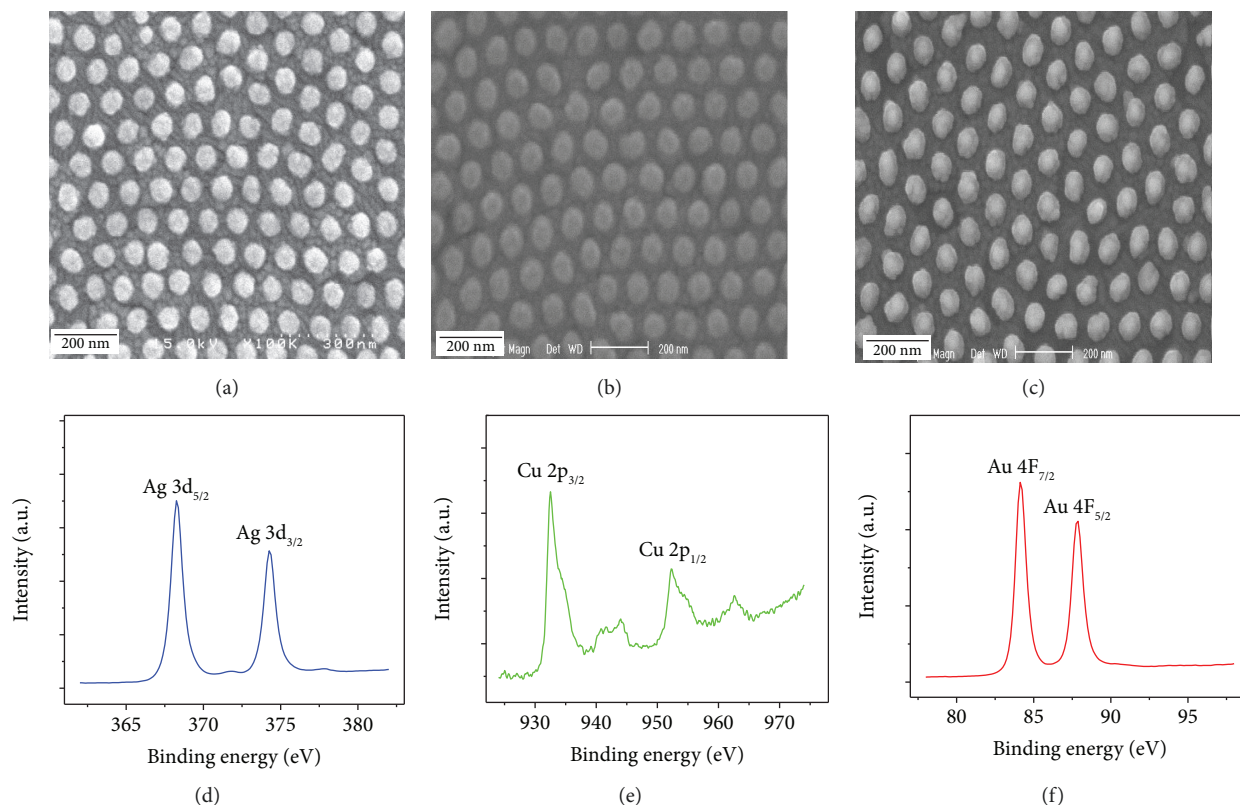
FIGURE 6: FE-SEM images of (a) Ag, (b) Cu, and (c) Au NDA with a diameter of 80 nm. The XPS spectra obtained from (d) 3d levels of Ag NDA, (e) 2p levels of Cu NDA, and (c) 4f levels of Au NDA.
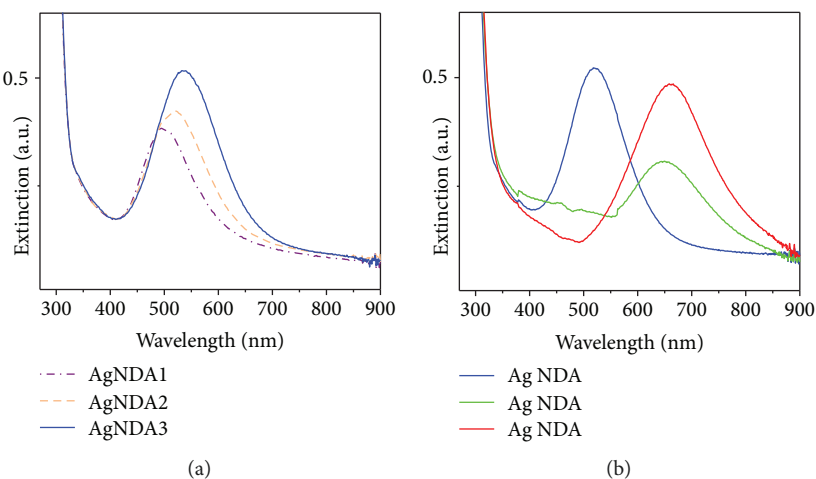

FIGURE 7: Extinction spectra of (a) Ag NDAs with different dot sizes (AgNDA1: $D = 42$ nm, AgNDA2: $D = 60$ nm, and AgNDA2: $D = 80$ nm) and (b) Ag, Cu, and Au NDAs with a similar dot diameter ($D = \sim 80$ nm).

of the Cu and Au NDAs, the maximum peaks were shown at 648 nm and 673 nm, respectively. The LSPR peak of the Ag NDAs was observed at a shorter wavelength than those of the Cu and Au NDAs. This result is consistent with the trends of peak positions of the LSPR from Ag and Au nanoparticles [40].

The LSPR of metal NDAs prepared using AAO masks has mainly focused on Ag or Au NDAs of different heights

with similar pore diameters [24–26]. Au NDAs of different heights (25, 40, 60, and 80 nm) with a similar dot diameter of 55 nm were fabricated on quartz plates, and the LSPR peaks are located at 700, 650, 620, and 585 nm [24]. The positions of LSPR peaks show a blue shift upon increasing the height of Au NDAs. Ag NDAs of different heights (75, 45, and 25 nm) with a similar dot diameter of 65 nm (±4 nm) were fabricated on the glasses, and the LSPR

peaks are observed at 433, 452, and 502 nm. The peak positions of the Ag NDAs with $\sigma = 0.88$, 1.56, and 2.44 shift to higher wavelengths as the aspect ratio increases [25]. The calculated peak broadening is smaller than the experimental width of the LSPR peak for the Ag NDA on the glass substrates. This is due to the dispersion of geometrical dimensions of the nanodots in the actual samples [25, 38]. The LSPR characteristics of metal NDAs are significantly affected by the substrate, metal deposition conditions, and the aspect ratio of the AAO mask [6, 20]. In addition, the LSPR in conductive metal oxide nanoparticles and in vacancy-doped semiconductor quantum dots is strongly influenced by the free electron carrier density [41, 42]. Since LSPR wavelengths are affected by various factors such as the nanoparticle size, composition, and substrate, free electron carrier density, more experiments should be systematically conducted to explore the LSPR in many material systems. To do this, reproducible manufacturing techniques of AAO masks are important. In the conventional wet etching process, the immersion time required for the pore opening of the AAO layer was difficult to control well owing to a slight difference in the thickness of the AAO barrier layer [29]. The etching rate may vary depending on the diffusion rate of the acid and depending on the shape of the surface, and hence even though there is a very small difference in height, the shape of the pores is significantly affected by etching for a long time [30]. A conventional chemical wet etching method for a long time results in the pore opening of the alumina barrier layer, but the pore wall of the AAO layer is sometimes collapsed. By using a two-step wet etch process, it was possible to achieve the pore opening in a short time without breaking the pore wall of the AAO layer, and it was possible to stably and reproducibly prepare AAO masks with size-controlled pores.

4. Conclusions

We demonstrated reproducible fabrication and plasmonic properties of size-controlled plasmonic NDAs using AAO masks. Large-area nanoporous alumina masks were achieved by a two-step wet etching process. The pore diameter of the AAO mask can be reproducibly controlled in the range of the hexagonal cell size by varying the immersing time of the second chemical wet etching. The dot diameter of the metal nanodot array depends on the AAO mask used as the evaporation mask. The LSPR spectra of Ag NDAs with different sizes (42 nm, 60 nm, and 80 nm) showed the maximum peak at 498 nm, 516 nm, and 533 nm and shifted to the red region as the dot diameter increased. The LSPR spectra for the Ag, Cu, and Au NDAs with a similar diameter of approximately 80 ± 5 nm indicated the maximum peaks at 533 nm, 648 nm, and 673 nm. These AAO masks could be utilized as a versatile mask to manufacture various 2D plasmonic NDAs.

Data Availability

All the data supporting the results are shown in the paper and are available from the corresponding author upon request.

Conflicts of Interest

There are no conflicts to declare.

References

[1] M. Jung, D. Mo Yoon, M. Kim et al., "Enhancement of hole injection and electroluminescence by ordered Ag nanodot array on indium tin oxide anode in organic light emitting diode," *Applied Physics Letters*, vol. 105, no. 1, article 013306, 2014.

[2] O. Vazquez-Mena, T. Sannomiya, L. G. Villanueva, J. Voros, and J. Brugger, "Metallic nanodot arrays by stencil lithography for plasmonic biosensing applications," *ACS Nano*, vol. 5, no. 2, pp. 844–853, 2011.

[3] Y. Lin, Y. Zou, Y. Mo, J. Guo, and R. G. Lindquist, "E-beam patterned gold nanodot arrays on optical fiber tips for localized surface plasmon resonance biochemical sensing," *Sensors*, vol. 10, no. 10, pp. 9397–9406, 2010.

[4] T. R. Jensen, M. D. Malinsky, C. L. Haynes, and R. P. van Duyne, "Nanosphere lithography: tunable localized surface plasmon resonance spectra of silver nanoparticles," *The Journal of Physical Chemistry B*, vol. 104, no. 45, pp. 10549–10556, 2000.

[5] K. L. Kelly, E. Coronado, L. L. Zhao, and G. C. Schatz, "The optical properties of metal nanoparticles: the influence of size, shape, and dielectric environment," *Physical Chemistry B*, vol. 107, no. 3, pp. 668–677, 2003.

[6] M. Duval Malinsky, K. L. Kelly, G. C. Schatz, and R. P. van Duyne, "Nanosphere lithography: effect of substrate on the localized surface plasmon resonance spectrum of silver nanoparticles," *The Journal of Physical Chemistry B*, vol. 105, no. 12, pp. 2343–2350, 2001.

[7] A. J. Haes and R. P. Van Duyne, "A nanoscale optical biosensor: sensitivity and selectivity of an approach based on the localized surface plasmon resonance spectroscopy of triangular silver nanoparticles," *Journal of the American Chemical Society*, vol. 124, no. 35, pp. 10596–10604, 2002.

[8] K. A. Willets and R. P. Van Duyne, "Localized surface plasmon resonance spectroscopy and sensing," *Annual Review of Physical Chemistry*, vol. 58, no. 1, pp. 267–297, 2007.

[9] J. N. Anker, W. P. Hall, O. Lyandres, N. C. Shah, J. Zhao, and R. P. van Duyne, "Biosensing with plasmonic nanosensors," *Nature Materials*, vol. 7, no. 6, pp. 442–453, 2008.

[10] P. J. Jesuraj and K. Jeganathan, "Improved hole injection in organic light emitting devices by gold nanoparticles," *RSC Advances*, vol. 5, no. 1, pp. 684–689, 2015.

[11] F. Liu and J.-M. Nunzi, "Enhanced organic light emitting diode and solar cell performances using silver nano-clusters," *Organic Electronics*, vol. 13, no. 9, pp. 1623–1632, 2012.

[12] C. Y. Cho, S. J. Lee, J. H. Song et al., "Enhanced optical output power of green light-emitting diodes by surface plasmon of gold nanoparticles," *Applied Physics Letters*, vol. 98, no. 5, article 051106, 2011.

[13] I. Lee, J. Y. Park, K. Hong, J. H. Son, S. Kim, and J.-L. Lee, "The effect of localized surface plasmon resonance on the emission color change in organic light emitting diodes," *Nanoscale*, vol. 8, no. 12, pp. 6463–6467, 2016.

[14] H. J. Kim, S. H. Lee, A. A. Upadhye et al., "Plasmon-enhanced photoelectrochemical water splitting with size-controllable gold nanodot arrays," *ACS Nano*, vol. 8, no. 10, pp. 10756–10765, 2014.

[15] Y. Xiong, R. Long, D. Liu et al., "Solar energy conversion with tunable plasmonic nanostructures for thermoelectric devices," *Nanoscale*, vol. 4, no. 15, pp. 4416–4420, 2012.

[16] S. Zou and G. C. Schatz, "Silver nanoparticle array structures that produce giant enhancements in electromagnetic fields," *Chemical Physics Letters*, vol. 403, no. 1–3, pp. 62–67, 2005.

[17] Y. Chu, E. Schonbrun, T. Yang, and K. B. Crozier, "Experimental observation of narrow surface plasmon resonances in gold nanoparticle arrays," *Applied Physics Letters*, vol. 93, no. 18, article 181108, 2008.

[18] U. Guler and R. Turan, "Effect of particle properties and light polarization on the plasmonic resonances in metallic nanoparticles," *Optics Express*, vol. 18, no. 16, pp. 17322–17338, 2010.

[19] P. A. Mistark, S. Park, S. E. Yalcin et al., "Block-copolymer-based plasmonic nanostructures," *ACS Nano*, vol. 3, no. 12, pp. 3987–3992, 2009.

[20] Y. Lei and W.-K. Chim, "Shape and size control of regularly arrayed nanodots fabricated using ultrathin alumina masks," *Chemistry of Materials*, vol. 17, no. 3, pp. 580–585, 2005.

[21] M. Jung, W. A. el-Said, and J. W. Choi, "Fabrication of gold nanodot arrays on a transparent substrate as a nanobioplatform for label-free visualization of living cells," *Nanotechnology*, vol. 22, no. 23, article 235304, 2011.

[22] H. Masuda and M. Satoh, "Fabrication of gold nanodot array using anodic porous alumina as an evaporation mask," *Japanese Journal of Applied Physics*, vol. 35, Part 2, No. 1B, pp. L126–L129, 1996.

[23] T. Kondo, H. Masuda, and K. Nishio, "SERS in ordered array of geometrically controlled nanodots obtained using anodic porous alumina," *Journal of Physical Chemistry C*, vol. 117, no. 6, pp. 2531–2534, 2013.

[24] F. Matsumoto, M. Ishikawa, K. Nishio, and H. Masuda, "Optical properties of long-range- ordered, high-density gold nanodot arrays prepared using anodic porous alumina," *Chemistry Letters*, vol. 34, no. 4, pp. 508-509, 2005.

[25] I.-C. Chen, Y. H. Chen, Y. C. Wang, and M. H. Shih, "Plasmon resonance properties of silver-patterned glass substrates fabricated by anodic alumina oxide templates," *Applied Physics A*, vol. 112, no. 2, pp. 381–386, 2013.

[26] T. Kondo, F. Matsumoto, K. Nishio, and H. Masuda, "Surface-enhanced Raman scattering on ordered gold nanodot arrays prepared from anodic porous alumina mask," *Chemistry Letters*, vol. 37, no. 4, pp. 466-467, 2008.

[27] Y. Wang, Y. Wang, H. Wang et al., "Hierarchical ultrathin alumina membrane for the fabrication of unique nanodot arrays," *Nanotechnology*, vol. 27, no. 2, article 025302, 2016.

[28] C. Y. Han, G. A. Willing, Z. Xiao, and H. H. Wang, "Control of the anodic aluminum oxide barrier layer opening process by wet chemical etching," *Langmuir*, vol. 23, no. 3, pp. 1564–1568, 2007.

[29] H. Robatjazi, S. M. Bahauddin, L. H. Macfarlan, S. Fu, and I. Thomann, "Ultrathin AAO membrane as a generic template for sub-100 nm nanostructure fabrication," *Chemistry of Materials*, vol. 28, no. 13, pp. 4546–4553, 2016.

[30] G. Meng, T. Yanagida, K. Nagashima et al., "Facile and scalable patterning of sublithographic scale uniform nanowires by ultrathin AAO free-standing membrane," *RSC Advances*, vol. 2, no. 28, pp. 10618–10623, 2012.

[31] P. Prieto, V. Nistor, K. Nouneh, M. Oyama, M. Abd-Lefdil, and R. Díaz, "XPS study of silver, nickel and bimetallic silver–nickel nanoparticles prepared by seed-mediated growth," *Applied Surface Science*, vol. 258, no. 22, pp. 8807–8813, 2012.

[32] X. Wang, J. C. Yu, C. Ho, and A. C. Mak, "A robust three-dimensional mesoporous ag/TiO$_2$ nanohybrid film," *Chemical Communications*, no. 17, pp. 2262–2264, 2005.

[33] Z. Jin, C. Liu, K. Qi, and X. Cui, "Photo-reduced Cu/CuO nanoclusters on TiO$_2$ nanotube arrays as highly efficient and reusable catalyst," *Scientific Reports*, vol. 7, no. 1, article 39695, 2017.

[34] I. Najdovski, P. R. Selvakannan, and A. P. O'Mullane, "Electrochemical formation of Cu/Ag surfaces and their applicability as heterogeneous catalysts," *RSC Advances*, vol. 4, no. 14, pp. 7207–7215, 2014.

[35] W. Kautek and J. G. Gordon II, "XPS studies of anodic surface films on copper electrodes," *Journal of the Electrochemical Society*, vol. 137, no. 9, pp. 2672–2677, 1990.

[36] J. Hernandez, P. Wrschka, and G. S. Oehrlein, "Surface chemistry studies of copper chemical mechanical planarization," *Journal of the Electrochemical Society*, vol. 148, no. 7, pp. G389–G397, 2001.

[37] J. Radnik, C. Mohr, and P. Claus, "On the origin of binding energy shifts of core levels of supported gold nanoparticles and dependence of pretreatment and material synthesis," *Physical Chemistry Chemical Physics*, vol. 5, no. 1, pp. 172–177, 2003.

[38] S. L. Westcott, J. B. Jackson, C. Radloff, and N. J. Halas, "Relative contributions to the plasmon line shape of metal nanoshells," *Physical Review B*, vol. 66, no. 15, article 155431, 2002.

[39] H. I. Muri and D. R. Hjelme, "LSPR coupling and distribution of interparticle distances between nanoparticles in hydrogel on optical fiber end face," *Sensors*, vol. 17, no. 12, article 2723, 2017.

[40] G. H. Chan, J. Zhao, E. M. Hicks, G. C. Schatz, and R. P. van Duyne, "Plasmonic properties of copper nanoparticles fabricated by nanosphere lithography," *Nano Letters*, vol. 7, no. 7, pp. 1947–1952, 2007.

[41] J. M. Luther, P. K. Jain, T. Ewers, and A. P. Alivisatos, "Localized surface plasmon resonances arising from free carriers in doped quantum dots," *Nature Materials*, vol. 10, no. 5, pp. 361–366, 2011.

[42] M. Kanehara, H. Koike, T. Yoshinaga, and T. Teranishi, "Indium tin oxide nanoparticles with compositionally tunable surface plasmon resonance frequencies in the near-IR region," *Journal of the American Chemical Society*, vol. 131, no. 49, pp. 17736-17737, 2009.

The Scientific World Journal

Journal of Applied Chemistry

Journal of Nanomaterials

Scientifica

International Journal of Polymer Science

Advances in Chemistry

Advances in Physical Chemistry

International Journal of Analytical Chemistry

Hindawi

Submit your manuscripts at
www.hindawi.com

Advances in Condensed Matter Physics

Journal of Chemistry

International Journal of Biomaterials

Advances in High Energy Physics

Journal of Engineering

Journal of Nanotechnology

International Journal of Corrosion

Journal of Materials

BioMed Research International

Advances in Tribology

Advances in Materials Science and Engineering